Simultaneous Retrieval Algorithm of Water Cloud Optical and Microphysical Properties by High-Spectral-Resolution Lidar

Kai Zhang, Lingyun Wu, Daniel Rosenfeld, Detlef Müller, Chengcai Li, Chuanfeng Zhao, Eduardo Landulfo, Cristofer Jimenez, Shuaibo Wang, Xianzhe Hu, Weize Li, Xiaotao Li, Yao Sun, Sihan Liu, Lan Wu, Xueping Wan, Wentai Chen, Chong Liu, Jian Bai, Jing Li, Wenbo Sun, Sivakumar Venkataraman, Yudi Zhou, Zhiji Deng, Ming Liu, Miao Cheng, Zhewei Fu, Weilin Pan, and Dong Liu

Manuscript received 13 March 2024; revised 11 June 2024; accepted 16 June 2024. Date of publication 19 June 2024; date of current version 2 July 2024. This work was supported in part by the National Key Research and Development Program under Grant 2022YFB3901704, in part by Donghai Laboratory Preresearch Project under Grant DH2022ZY0003, and in part by the State Key Laboratory of Extreme Photonics and Instrumentation Innovation Program under Grant EPI2023ZD01. *(Corresponding author: Dong Liu.)*

Kai Zhang and Dong Liu are with the State Key Laboratory of Extreme Photonics and Instrumentation, College of Optical Science and Engineering, Zhejiang University, Hangzhou 310027, China, and also with the ZJU-Hangzhou Global Scientific and Technological Innovation Center, Zhejiang University, Hangzhou 311200, China (e-mail: 3150104660@zju.edu.cn; liudongopt@zju.edu.cn).

Lingyun Wu, Shuaibo Wang, Xianzhe Hu, Weize Li, Xiaotao Li, Yao Sun, Lan Wu, Chong Liu, Jian Bai, and Yudi Zhou are with the State Key Laboratory of Extreme Photonics and Instrumentation, College of Optical Science and Engineering, Zhejiang University, Hangzhou 310027, China (e-mail: wlyun@zju.edu.cn; wangshuaibo_opt@zju.edu.cn; 22130073@zju.edu.cn; lwz5514@zju.edu.cn; 22130017@zju.edu.cn; 22330028@zju.edu.cn; wul@zju.edu.cn; chongliu@zju.edu.cn; bai@zju.edu.cn; zhouyudi@zju.edu.cn).

Daniel Rosenfeld is with the Institute of Earth Sciences, The Hebrew University of Jerusalem, Jerusalem 91904, Israel (e-mail: daniel.rosenfeld@mail.huji.ac.il).

Detlef Müller is with the School of Remote Sensing and Information Engineering, Wuhan University, Wuhan 430072, China (e-mail: dgmueller@whu.edu.cn).

Chengcai Li, Chuanfeng Zhao, and Jing Li are with the Department of Atmospheric and Oceanic Sciences, School of Physics, Peking University, Beijing 100871, China (e-mail: ccli@pku.edu.cn; cfzhao@pku.edu.cn; jing-li@pku.edu.cn).

Eduardo Landulfo is with the Center for Lasers and Applications, Institute of Energy and Nuclear Research, São Paulo 05508-000, Brazil (e-mail: landulfo@gmail.com).

Cristofer Jimenez is with the Leibniz Institute for Tropospheric Research, 04318 Leipzig, Germany (e-mail: jimenez@tropos.de).

Sihan Liu is with the Satellite Application Center for Ecology and Environment, MEE, Beijing 100094, China (e-mail: liusihan1200@163.com).

Xueping Wan and Wentai Chen are with Wuxi CAS Photonics Company Ltd., Wuxi 214000, China (e-mail: Xueping_wan@cas-pe.com; wentai_chen@cas-pe.com).

Wenbo Sun is with Donghai Laboratory, Zhoushan 316021, China (e-mail: haitianyise@donghailab.com).

Sivakumar Venkataraman is with the School of Chemistry and Physics, Discipline of Physics, University of KwaZulu-Natal, Durban 4000, South Africa (e-mail: Venkataramans@ukzn.ac.za).

Zhiji Deng, Ming Liu, Miao Cheng, and Zhewei Fu are with Zhejiang Dahua Technology Company Ltd., Hangzhou 310053, China (e-mail: deng_zhiji@dahuatech.com; liu_ming@dahuatech.com; cheng_miao@dahuatech.com; fu_zhewei@dahuatech.com).

Weilin Pan is with the Institute of Atmospheric Physics, Chinese Academy of Sciences, Beijing 100029, China, and also with the College of Earth Sciences, University of Chinese Academy of Science, Beijing 101499, China (e-mail: panweilin@mail.iap.ac.cn).

Digital Object Identifier 10.1109/TGRS.2024.3416493

***Abstract*— The uncertainty of water cloud feedback on radiative forcing is one of the largest obstacles to producing confident projections of the global climate. Sufficient measurements of water clouds are crucial to addressing this issue. However, existing techniques based on remote sensing or in situ instruments face limitations in data capacity attributed to the short lifetime, high temporal variability, and complex vertical structure of water clouds. In this study, taking advantage of a dual-field-of-view (dual-FOV) high-spectral-resolution lidar (HSRL), we developed a novel algorithm to obtain diurnal simultaneous profiles of water cloud optical and microphysical properties with high temporal–spatial resolution. This technique does not rely on the widely used subadiabatic assumption about the vertical structure of water clouds. The retrieval algorithm, validated by simulations and cloud radar measurements, was applied to field experiment data collected at the Beijing and Hangzhou sites in China. The relationship functions between water cloud properties are presented to enhance our understanding of the underlying processes. Furthermore, the vertical distributions of retrieved properties are compared to the subadiabatic assumption. The dual-FOV HSRL technique enables comprehensive observations, enhancing our understanding of water clouds and providing significant insights into the interactions among clouds, aerosols, precipitation, and radiation.**

***Index Terms*— Dual-field-of-view (dual-FOV) high-spectral-resolution lidar (HSRL), multiple scattering, properties, vertical structure, water clouds.**

I. Introduction

WATER clouds are of great environmental importance as a primary source of uncertainty in model projection of global climate change [1], [2], [3]. Changes in water cloud coverage can result in significant variations in global warming [4], [5]. Complex aerosol–cloud interaction is a primary component of uncertainty of the historical radiative forcing of Earth's climate [6], [7]. Intermodel differences in simulating the aerosol–cloud interaction represent a substantial source of uncertainty in predicting future climate change [8]. Furthermore, the formation and growth of water cloud droplets can impact precipitation chemistry, affect the hydrological cycle on Earth, and influence ecosystems [9], [10]. Determining the optical and microphysical properties of water clouds, along with their internal structure, is crucial for evaluating

their climate impact and understanding the mechanisms of interactions between aerosols, clouds, and precipitation.

However, the short lifetime, high temporal variability, and complex vertical structure of water clouds pose a major difficulty for the existing observation techniques [11]. Airborne in situ observations provide comprehensive and detailed information on water cloud properties but have limitations in temporal and vertical coverage due to the duration of flights and unavoidable contact with clouds [12]. Despite their global coverage, the inability of passive sensors to measure vertical profiles leads to insufficient information about cloud distribution [13], [14]. Radars, such as CloudSat or ground-based cloud radar, provide cloud property profiles while having a limited spatial resolution for thin clouds [15].

Lidars provide an opportunity to capture profiles of water clouds with high temporal and spatial resolutions. In that way, lidar is a valuable complement to other cloud-detection methods. Utilizing the multiple-scattering affected signals (multiple-scattering signals) obtained by different receiver field-of-view (FOV), multiple-FOV lidar systems were developed to measure Mie scattering by water cloud droplets [16], [17], [18]. However, the inhomogeneous Mie-scattering phase function presents challenges in accurately quantifying water cloud properties. To overcome this conundrum, a dual-FOV (dual-FOV) Raman lidar was employed for water cloud observations benefitting from Raman scattering phase function [19], [20]. A challenge lies in the fact that Raman signals with low signal-to-noise ratios are restricted to nighttime observations, thus constraining their usability [21]. The understanding of diurnal variations of clouds is important to the determination of Earth's radiation budget [22]. The constraints of Raman lidar observations could be partially solved by the development of the polarization lidar technique. This technique allows for retrieving water cloud properties from polarization ratios of the measured signals [23], [24]. Nevertheless, this method relies on the subadiabatic assumption, which is, however, inconsistent with reality [25]. Therefore, while the available observation methods have their strengths and weaknesses, there is still a deficiency in effectively detecting water clouds with high temporal–spatial resolution on a diurnal basis.

To address this issue, the high-spectral-resolution lidar (HSRL) technique effectively distinguishes molecular (Rayleigh) and particle (Mie) scattering signals by employing a high-resolution spectral discriminator [26], [27]. Consequently, it allows for using the smooth and almost isotropic phase function of molecular scattering while simultaneously addressing the drawback of the Raman technique, i.e., the inability to perform during daytime conditions due to the weak Raman signals compared to the sky background. However, there has been limited research on the fundamental microphysical properties of clouds using HSRL observations, which primarily focus on the macroscopic physical and optical properties of clouds [28].

We have empirically demonstrated the valuable application of the dual-FOV HSRL technique in studying cloud–aerosol interaction [29]. In this study, we present a detailed exposition of the retrieval algorithm for water clouds using the dual-FOV HSRL. This technique enables diurnal, high temporal–spatial resolution, and simultaneous profiling of the extinction coefficient (α_c), the effective radius (r_{eff}), the liquid water content (LWC), and the cloud droplet number concentration (N_{d}) of water clouds without relying on the subadiabatic assumption. The retrieval results were validated by simulations and cloud radar products with great consistency. The retrieval algorithm was applied to measured data from field experiments conducted at the Beijing and Hangzhou sites in China, 39.98°N, 116.38°E, and 30.26°N, 120.12°E. In addition, the relationships between observed water cloud properties, as well as their vertical structure, are presented.

II. Materials and Methods

A. Dual-FOV HSRL System

The dual-FOV HSRL system operates an iodine vapor (I_2) absorption ultranarrow spectral filter at 532 nm [30]. A detailed description of the HSRL system can be found in previous work [29]. In the transmitting unit, a Nd-YAG laser emits linearly polarized laser pulses at 532 nm with a pulse energy of 100 mJ, a repetition rate of 10 Hz, and a divergence angle of 0.3 mrad [31]. The receiving unit incorporates two different FOVs for collecting lidar signals: a narrow FOV, adjustable between 0.36 and 1 mrad, and a wide FOV of 2 mrad. At the narrow FOV, a polarization beam splitter, followed by a beam splitter and an I_2 filter, separates the return signals into the perpendicular, parallel, and molecular detection channels. The perpendicular and parallel channels measure the intensity of total backscattering (the particulate and molecular backscattering signal) in perpendicular and parallel polarization states, while the molecular channel exclusively detects the molecular backscattering signal [26], [32]. With regard to the wide FOV, only a molecular channel is used. Signals from this channel are used to evaluate the multiple-scattering effects of photons in water clouds.

B. Forward Simulation Models for Water Cloud Signals

The HSRL signals are usually obtained from the conventional lidar equations [26]. Owing to the multiple-scattering effect of photons in water clouds, simulating signals of water clouds observed by HSRL are more complex.

The Monte Carlo (MC) method has been extensively utilized as a robust tool for the numerical simulation of lidar signals from water clouds, taking into account the multiple-scattering effect. This method is able to generate realistic results without the need for many assumptions, as previously described in more detail [33]. In this study, the semi-analytical MC method [34], [35] has been adapted for the simulation of HSRL signals, which are used as input signals to validate the performance of the subsequent retrieval algorithm. However, the MC method suffers from low computational efficiency, limiting its application in the retrieval of water cloud properties.

To overcome the shortage of the MC model, an analytical expression of multiple-scattering signals from water clouds has been proposed by Malinka and Zege [36]. This analytical

model (AM) can simulate lidar signals with high efficiency and relatively high accuracy, which is used as a forward simulation model for the retrieval of cloud properties. Since the original AM was used for Raman scattering signals, one needs to use the molecular (Rayleigh) scattering phase function to replace the Raman scattering phase function without wavelength conversion. The molecular scattering phase function can be expressed as [35]

$$P_m(\theta) = \frac{3\left(1 + p\cos^2\theta\right)}{4\pi(3+p)} \tag{1}$$

where p is the polarization parameter, which is usually equal to one.

The atmospheric conditions for running the simulated signal profile refer to U.S. Standard Atmosphere [37]. When comparing the simulated signal with the measured signal, signals are normalized by the signal intensity at the cloud base.

C. Retrieval of Water Cloud Properties

Before presenting the water cloud retrieval algorithm, it is first necessary to define the particle size distribution and related key properties of water clouds. In this study, the widely used gamma distribution is adopted as the parameterization solution for the size distribution of water cloud droplets (see Appendix for more details). The (single scattering) extinction coefficient (α_c) and the effective droplet radius (r_{eff}) act as the two most critical properties in water cloud retrieval [23], [38]. All water cloud extinction coefficients α_c in this work are values in the single-scattering condition. Based on α_c and r_{eff}, the LWC and the cloud droplet number concentration (N_{d}) of water clouds can be derived [24].

The retrieval of water cloud properties with the dual-FOV HSRL is based on the premise that the measured molecular signals (B_{M}) exhibit varying intensities at differing FOVs. This is because the multiple-scattering effect of photons in water clouds affects the count and angular distribution of photons received by lidar, which is decided by α_c and the scattering phase function of water clouds [39]. r_{eff} can be derived by its correlation with the scattering phase function. Although the molecular channel detects the frequency-shifted part of Rayleigh scattering, this part of the signals is also subjected to multiple scattering by clouds. Hence, the intensity of the molecular channel signal also varies at different FOVs due to the multiple-scattering effect in water clouds, containing the necessary information for the retrieval of the water cloud properties. Thus, by utilizing signals from two different FOVs of HSRL, α_c and r_{eff} can be retrieved with an iterative retrieval scheme and subsequently used to derive LWC and N_{d}, as shown in Fig. 1. This method does not rely on the subadiabatic assumption and is able to work diurnally benefiting from the relatively high intensity of HSRL signals during daylight hours. The following is a detailed description of the algorithmic flow.

1) The simulated molecular signal (B_{S}) at height z above HSRL can be simulated by the AM [23], [39]

$$B_{\text{S}}(z) = F[C, \alpha_c(z), r_{\text{eff}}(z), \varphi] \tag{2}$$

where F represents the forward simulation of the lidar signals by the AM, C is the lidar system constant, and φ is the width of FOV.

2) We analyze the quantitative relationship between signal differences and differences in water cloud properties. The sensitivity of B_{S} at height z_i (SC_x) to the water cloud properties at the height z_j ($z_i \geq z_j$) is defined as

$$\text{SC}_x(z_i, z_j) = \frac{x(z_j)}{B_S(z_i)} \frac{dB_S(z_i)}{dx(z_j)} \tag{3}$$

where x represents one of the critical water cloud properties (α_c or r_{eff}). The sensitivity relates the difference between the simulated and measured signals to the difference between the water cloud properties for the simulation and the actual water cloud properties. This connection is a crucial tool for the following retrieval of water cloud properties. By setting a small change in the water cloud properties input for the AM, the corresponding signal sensitivity SC_x can be obtained by the signal variations in forward simulations. It is worth noting that SC_x needs to be calculated and updated at each iteration.

3) By correcting the water cloud properties in (2), the relative differences between the simulated signal profiles and the measured ones can be reduced. Equation (3) can be rewritten to

$$\frac{\Delta B_{\text{S}}}{B_{\text{S}}} = \frac{\Delta x}{x}\text{SC}_x \tag{4}$$

where ΔB_{S} represents the difference between B_{S} and B_{M}, and Δx is the difference between the water cloud properties for the simulation and the actual water cloud properties. This equation works as the correction step that allows us to converge the water cloud properties for the simulation to the actual ones. The correction step of α_c and r_{eff} can be solved from (4) as

$$\begin{aligned}\Delta\mathbf{X} &= \begin{bmatrix} \frac{\Delta\alpha_c}{\alpha_c} & \frac{\Delta r_{\text{eff}}}{r_{\text{eff}}} \end{bmatrix} \\ &= \begin{bmatrix} \frac{\Delta B_{\text{S1}}}{B_{\text{S1}}} & \frac{\Delta B_{\text{S2}}}{B_{\text{S2}}} \end{bmatrix} \begin{bmatrix} \text{SC}_{\alpha_c,1} & \text{SC}_{\alpha_c,2} \\ \text{SC}_{r_{\text{eff}},1} & \text{SC}_{r_{\text{eff}},2} \end{bmatrix}^{-1} \\ &= \Delta\mathbf{B} \cdot \mathbf{SC}^{-1} \end{aligned} \tag{5}$$

where superscript -1 represents the generalized inverse matrix and subscripts 1 and 2 correspond to the narrow FOV and wide FOV, respectively.

It should be noted that the parameters in (4) and (5) describe their whole profiles because a profile of the lidar signal of the water cloud is jointly determined by α_c and r_{eff} at all heights. Then, B_{S} can be resimulated by the corrected α_c and r_{eff} to reduce ΔB_{S}. In order to mitigate the risk of overfitting, we utilize the damped singular value decomposition method as a regularization technique to solve (5), with the regularization parameter chosen by generalized cross validation [40]. This solution offers more robust retrieval results when we compare it to alternative regularization methods and parameter selections.

4) Due to the presence of signal noise, even if the water cloud properties are identical, there will still be differences between the simulated and measured signals. Therefore, the correction will be iterated until ΔB_{S} falls within predetermined thresholds that depend on the signal-to-noise ratio of the

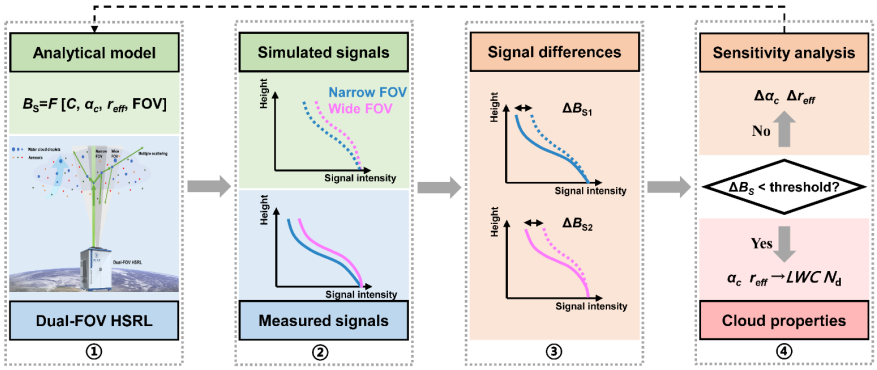

Fig. 1. Flowchart of the iterative retrieval scheme for water cloud products of the dual-FOV HSRL.

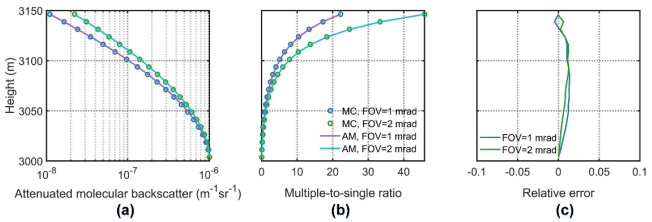

Fig. 2. Comparison between simulated results by the MC model and the AM. (a) Attenuated molecular backscatters. (b) Ratios of multiple scattering signals to single-scattering signals. (c) Relative deviations between MC and AM signals.

specific dual-FOV HSRL system (signal relative difference values of 5% in this work). At this time, the water cloud properties input in (2) are regarded as the final retrieval results.

III. Results and Discussion

A. Comparison of Forward Simulation Models

The consistency of the MC and analytical simulation models is compared by simulating a water cloud scenario. A subadiabatic water cloud (α_c and r_{eff} are 0.028 m^{-1} and 9.5 μm at the reference height, respectively; height from 2010 to 2310 m above ground level) was used in the simulations. The parameterization of the subadiabatic water cloud is given in Appendix A. The FOV was equal to 1 and 2 mrad to consider different FOVs and the spatial resolution is 7.5 m. The simulated molecular signals are shown and compared in Fig. 2. Since background aerosols outside the cloud normally produce negligible multiple-scattering signals, only attenuated backscatters (independent of the system constant) obtained by molecular detection channels inside the cloud were studied in this ideal simulation.

As depicted in Fig. 2(a) and (b), there are significant differences in the intensities of simulated signals and their multiple-scattering components at different FOVs. In addition, Fig. 2(b) shows that the influence of multiple-scattering effects within the water cloud intensifies with greater penetration depth and FOV. As presented in Fig. 2(c), the analytical method slightly overestimates multiple-scattering signals, but the relative signal deviations between these two models generally remain below 2%. These findings suggest that the AM achieves comparable simulation accuracy to the widely employed MC model while having remarkable computational efficiency for retrieving water cloud properties.

TABLE I

Parameterization of the MC Simulations. The Vertical Structure of the Input Cloud Model Is Based on the Subadiabatic Assumption

Parameters	Value (unit)
HSRL	
Laser wavelength	532 nm
Narrow FOV	1 mrad
Wide FOV	2 mrad
Spatial resolution	7.5 m
Water cloud	
Cloud height range	2002.5~2152.5 m
Reference height	2077.5 m
α_c at the reference height	0.01~0.03 m-1
r_{eff} at the reference height	8~16 μm

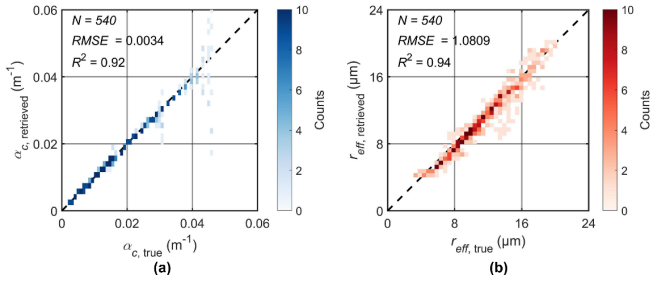

Fig. 3. Performance of the dual-FOV HSRL technique. (a) Comparisons of retrieved cloud extinction coefficient $\alpha_{c,\text{retrieved}}$ with MC inputs $\alpha_{c,\text{true}}$. (b) Comparisons of retrieved cloud droplet effective radius $r_{\text{eff,retrieved}}$ with MC inputs $r_{\text{eff,true}}$.

B. Performance of Retrieval Algorithm

The performance of the dual-FOV HSRL technique is evaluated by MC simulations of lidar signals by water clouds. The parameterization details of the MC simulations are given in Table I.

As shown in Fig. 3, the retrieved values of α_c and r_{eff} agree well with the true values. Values of the root-mean-square error (RMSE) of α_c and r_{eff} are 0.0034 and 1.0809, respectively. The coefficients of determination (R^2) are 0.92 and 0.94. Notably, relatively higher α_c values result in larger retrieval errors, which can be attributed to the stronger multiple-scattering effects that reduce the signal-to-noise ratio of simulated signals from the MC model.

The stochastic fluctuations of MC simulation signals effectively capture the impact of noise interference on the measured

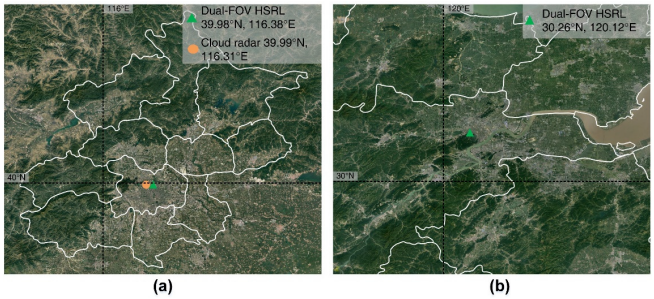

Fig. 4. Locations of (a) HSRL and the cloud radar at the Beijing site and (b) HSRL at the Hangzhou site.

signal. Consequently, it can be anticipated that the retrieval error will gradually increase as optical thickness increases. The signal-to-noise ratio will therefore decrease in the retrieval of real signals.

Nevertheless, α_c values as large as the maximum values set in our simulations are unlikely to occur frequently. Results show that the dual-FOV HSRL technique allows for achieving accurate retrieval results within the effective signal range of lidar detections.

C. Case Study

To demonstrate the performance and applicability of the proposed method, case studies of water clouds were conducted using the dual-FOV HSRL system. Atmospheric cloud and aerosol observations were carried out at the Beijing site (39.98°N, 116.38°E) from January 22, 2021, to April 18, 2021, and the Hangzhou site (30.26°N, 120.12°E) from January 10, 2023, to May 13, 2023.

Fig. 4 shows the locations of observations. Two water cloud episodes were selected from each observation site, and the retrieval results are presented in Fig. 3. The retrieved properties have a temporal resolution of 5 min and a spatial resolution of 7.5 m.

The scattering ratio R_a of the water cloud, i.e., the backscattering intensity of water clouds (or aerosols) over that of atmospheric molecules, was significantly higher compared to the background aerosols. Fig. 5(b) shows that the depolarization ratio inside the water cloud increases with height due to the multiple-scattering effect, which is consistent with previous studies [27]. In the actual retrieval process, certain regions were excluded from the retrieval analysis. These included higher regions of clouds for which laser penetration depth (around 100 $\sim$ 200 m in these cases) was limited and optically thin portions near the cloud base where the multiple-scattering effects are negligible (i.e., small differences in the dual-FOV signals make retrievals difficult). In addition, regions where the overlap between the laser beam and receiver FOV was incomplete were also excluded from the retrieval process [41]. Consequently, effective height ranges for which cloud properties were obtained in Fig. 5(c)–(f) are smaller than the true geometrical extent of a cloud.

Overall, the extinction coefficient α_c, effective droplet radius r_{eff}, and LWC of water clouds increase with height, while the cloud droplet number concentration N_{d} remains relatively stable with height. Temporal variations in water

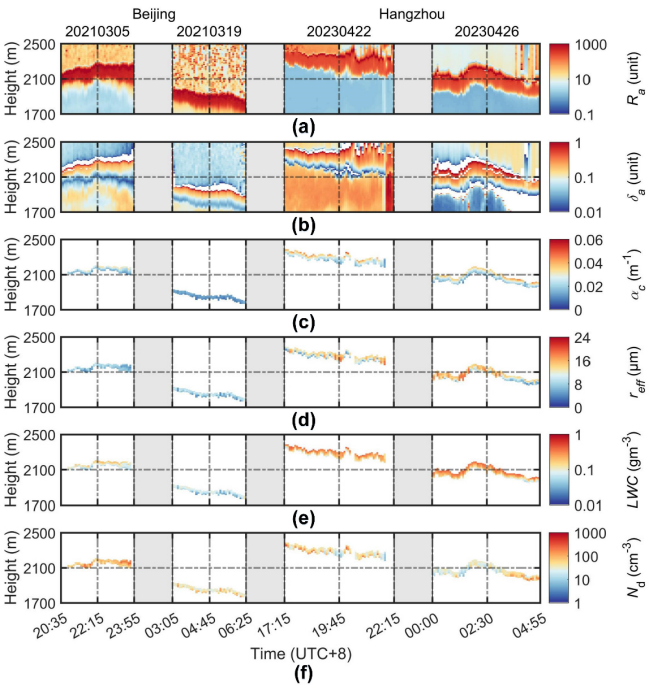

Fig. 5. HSRL observations of water clouds in Beijing and Hangzhou. (a) Scattering ratio R_a at 532 nm. (b) Depolarization ratio δ_a at 532 nm. (c) Cloud extinction coefficient α_c at 532 nm. (d) Cloud droplet effective radius r_{eff}. (e) LWC. (f) Cloud droplet number concentration N_{d}.

cloud properties can also be observed, as the results are showing for the Hangzhou site on April 26, 2023. There was a significant increase in N_{d} and a decrease in r_{eff} of the water cloud after 3:00 (local time, universal time coordinated (UTC) + 8). Differences in the optical and microphysical properties of water clouds were found between the two observation sites in similar seasonal and altitude conditions. Specifically, the cloud LWC at the Hangzhou site (an average value of 0.229 gm^{-3}) was observed to be greater than that at the Beijing site (an average value of 0.086 gm^{-3}), which aligns with previous findings [42], [43]. The similarity in N_{d} of the water clouds at the two sites suggests that this difference stems from the size of the water cloud droplets. We found that r_{eff} of the water clouds at the Hangzhou site (an average value of 12.3 μm) is larger than that at the Beijing site (an average value of 7.8 μm). Relative humidity and specific cloud LWC from ERA5 reanalysis data are included to corroborate these findings (Fig. 6). This difference is mainly because the different relative humidities in these two sites foster different liquid water lapse rates [44]. The results from the case studies further demonstrate the ability of the dual-FOV HSRL technique in quantifying the value and vertical distribution of water cloud properties.

In addition, to demonstrate the practical performance of the dual-FOV HSRL technique, we conducted simultaneous measurements using a 33.44-GHz cloud radar located near the Beijing site (39.99°N, 116.31°E, approximately 6 km away) for the water cloud case on March 5, 2021. Although a spatial distance existed between the HSRL and the cloud radar, this distance is significantly smaller than the typical horizontal scale range of low-level water clouds [45], [46]. Thus, despite some differences, the observed properties of water clouds by

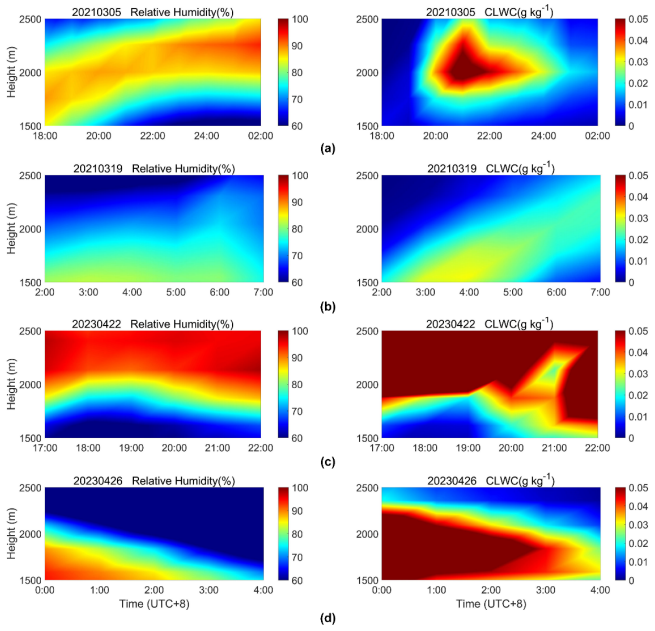

Fig. 6. Relative humidity and specific cloud liquid water content (CLWC) from ERA5 on (a) March 5, 2021 at the Beijing site; (b) March 19, 2021 at the Beijing site; (c) April 22, 2023 at the Hangzhou site; and (d) April 26, 2023 at the Hangzhou site.

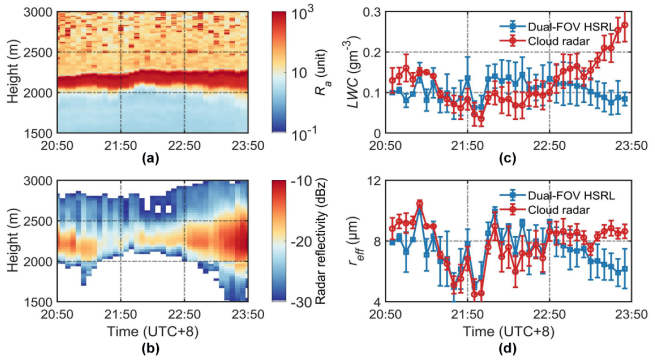

Fig. 7. Comparison of dual-FOV HSRL products with the cloud radar on March 5, 2021. (a) Scattering ratio R_d at 532 nm observed by the dual-FOV HSRL. (b) Radar reflectivity observed by the cloud radar. (c) Comparison of the vertical mean values of LWC obtained by the dual-FOV HSRL with the cloud radar. (d) Comparison of the vertical mean values of r_{eff} obtained by the dual-FOV HSRL with the cloud radar. The error bars stand for the standard deviations of the averaged values.

these two instruments were comparable. The data processing of cloud radar is given in Appendix B.

Fig. 7 shows the simultaneous observation of the water cloud layer at the same height obtained from the dual-FOV HSRL and the radar. Fig. 7(a) and (b) presents the comparison between the cloud scattering ratio and radar reflectivity. The height and undulation of the cloud base detected by both instruments were generally consistent. The water cloud thickness detected by the cloud radar is greater than that detected by HSRL as the penetration depth of the laser beam into the cloud is limited.

Furthermore, Fig. 7(c) and (d) presents a comparison of LWC and r_{eff} obtained from the two measurements. Given the different spatial resolutions and penetration depths of the two techniques, both LWC and r_{eff} were vertically averaged within

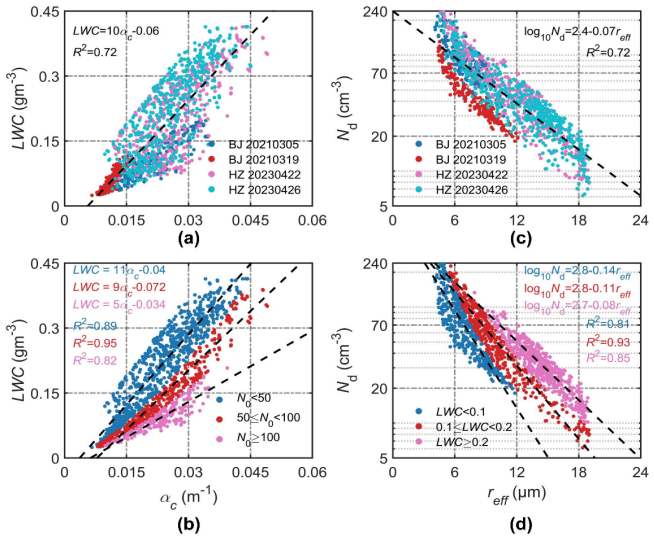

Fig. 8. (a) Relationship between cloud extinction coefficient α_c at 532 nm and LWC. (b) Relationship between α_c at 532 nm and LWC for different height bins of N_{d}. (c) Relationship between cloud droplet effective radius r_{eff} and cloud droplet number concentration N_{d}. (d) Relationship between r_{eff} and N_{d} for different height bins of LWC. Different colors of data points are used for different water cloud cases. BJ represents the Beijing site and HZ represents the Hangzhou site. The total number of data points is 1470, of which 224, 234, 452, and 560 are for the four days in (a) and (c), while 456, 416, and 598 are for the three cases in (b) and (d), respectively.

effective height intervals of the dual-FOV HSRL products. As shown in Fig. 7(c) and (d), there was a temporal fluctuation of the water cloud properties, which is a typical behavior in well-developed and preexisting water clouds [47]. The results exhibit good agreement between 20:50 and 23:20 UTC + 8, thereby confirming the consistency and accuracy of the retrieved water cloud properties.

The vertical extent and water cloud properties observed by the dual-FOV HSRL and radar instruments showcase their respective advantages during specific time intervals. Around 21:50 UTC + 8, the LWC and r_{eff} of the water cloud were relatively minimal. During this period, the dual-FOV HSRL exhibited enhanced sensitivity to small cloud droplets, whereas the radar failed to detect the cloud base, as shown in Fig. 7(c). Between 23:20 and 23:50 UTC + 8, the radar successfully identified a broader vertical extent of the water cloud. Concurrently, the radar-derived LWC and r_{eff} surpassed those retrieved by the dual-FOV HSRL. Radar's greater penetration depth enables it to pinpoint the actual cloud top. Moreover, the possible presence of drizzle in water clouds in this period of time resulted in higher radar-derived LWC and r_{eff} values compared to the HSRL, which has lower sensitivity to larger particles.

D. Relationship Between Retrieved Water Cloud Properties

With the observation data at the Beijing and Hangzhou sites (see Fig. 5), a statistical analysis of the relationship between water cloud properties can be performed. Fig. 8(a) and (b) shows the relationship between the LWC and the extinction coefficient α_c. The equations can be written as $\text{LWC} = m_1\alpha_c - n_1$, with the coefficients m_1 and n_1 of the equations provided in Fig. 8(a) and (b). This analysis reveals a linear positive

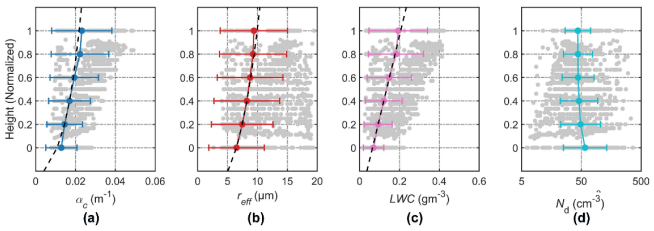

Fig. 9. Height-normalized water cloud properties. (a) Cloud extinction coefficient α_c at 532 nm. (b) Cloud droplet effective radius r_{eff}. (c) LWC. (d) Cloud droplet number concentration N_{d}. The value 0 represents the lowest height of the retrieved profiles, whereas 1 represents the largest retrievable height limited by the penetration depth of laser. The total number of data points (gray) is 1470. The colored points represent the mean values and the length of the bars represent the standard deviation.

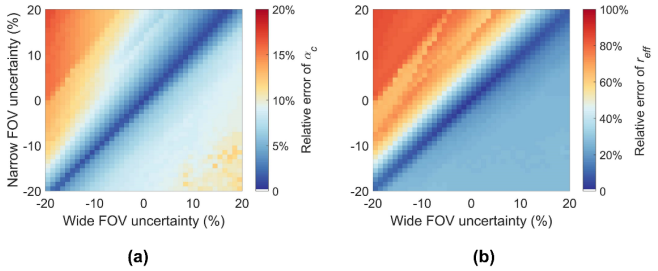

Fig. 10. Relative error of retrieved (a) cloud extinction coefficient α_c and (b) cloud droplet effective radius r_{eff} caused by FOV uncertainties.

correlation between these two variables. As shown in Fig. 8(b), the relationships are more significant for different height bins of N_{d}, with values of R^2 increasing from 0.72 to a range of 0.82 $\sim$ 0.92. Consequently, this correlation implies that the water cloud extinction coefficient can serve as a valuable indicator for estimating the LWC of the cloud, particularly in cases where N_{d} is fixed [48].

Fig. 8(c) and (d) depicts the relationship between cloud droplet number concentration N_{d} and effective radius r_{eff}. N_{d} decreases significantly as r_{eff} grows, indicating a linear negative correlation between $\log_{10}(N_{\text{d}})$ and r_{eff}. The relationship is $\log_{10}(N_{\text{d}}) = m_2 r_{\text{eff}} - n_2$ where the coefficients m_2 and n_2 are given in Fig. 8(c) and (d). The Twomey effect assumes that the vertically integrated LWC remains constant as the number of cloud condensation nuclei increases [49]. Consequently, an increased N_{d} would lead to a decrease in r_{eff} [50]. Similarly, relationships between N_{d} and r_{eff} become more pronounced for different height bins of LWC, as evidenced by the increase in R^2 values from 0.72 to a range of 0.81–0.93. The negative correlation highlights that larger droplets are usually associated with lower droplet number concentrations [51], [52].

The results presented in Fig. 8 suggest that accurate characterization of α_c and r_{eff} can provide crucial information for estimating LWC and N_{d}, respectively. These relationships summarized by dual-FOV HSRL data will provide important guidance for other, more common, and basic lidar systems (e.g., Mie scattering lidars) to evaluate water cloud properties. Although previous studies have discussed the relationship between water cloud properties [51], [52], [53], [54], the equations obtained from our linear regression analysis offer a valuable contribution to the understanding of low-level water clouds in North and East China.

E. Vertical Structure of Water Clouds

The retrieval results in Fig. 5 indicate a consistent increase in α_c, r_{eff}, and LWC with height, while N_{d} remains relatively constant in the vertical direction. To further analyze the vertical structures of water clouds, Fig. 9 presents height-normalized α_c, r_{eff}, and LWC along with their predicted vertical structures based on the subadiabatic assumption (represented by black dashed lines).

The results indicate that the measured data are generally consistent with the subadiabatic model in the lower region of the water clouds. However, slight variations are observed at greater penetration depths, as previously reported [55]. As there is enhanced entrainment of drier air near the cloud top, it is expected that natural water cloud properties would exhibit larger discrepancies compared to the subadiabatic assumption in the higher regions beyond the laser penetration depth. Therefore, it can be concluded that the subadiabatic assumption has good applicability for water cloud retrieval based on lidar with weaker penetration, and however, the increased deviation near the cloud top can be a limiting factor in the accuracy of the satellite retrievals [25].

F. Evaluation of FOV Uncertainties

The fundamental principle of the retrieval algorithm lies in the different multiple scattering intensities between two different FOVs, which provide critical information regarding water cloud properties. Therefore, the impact of FOV uncertainties (i.e., deviations between FOVs employed in retrieval and the actual FOVs) on the retrieval accuracy will be discussed in the following text.

For the dual-FOV HSRL system used in this work, the FOV uncertainty can be attributed to machining and hysteresis errors associated with the adjustable field stop. These errors add up to about 10% uncertainty in the width of the FOV. Detailed descriptions of the HSRL system can be found in our previous work [29], [41], and therefore, we do not focus on discussing the detail of the design of FOVs.

In this section, the MC model was used to simulate HSRL signals that can be obtained from the water cloud. A vertically homogenous water cloud ($r_{\text{eff}} = 9$ μm, narrow FOV = 1 mrad, wide FOV = 2 mrad, and other parameters are the same as in Fig. 2) was used in the simulations. In order to examine the impact of an FOV uncertainty on the retrieval of α_c and r_{eff}, a broader range of FOV uncertainties varying from 0 to $\pm 20\%$ was considered. Relative errors of the retrieved α_c and r_{eff} compared to the input α_c and r_{eff} of MC simulations are shown in Fig. 10.

The results demonstrate that the effect of FOV uncertainty is more pronounced on r_{eff} compared to α_c. Furthermore, when the uncertainty in the narrow FOV exceeds that of the wide FOV (orange area in Fig. 10), the retrieved α_c and r_{eff} exhibit significantly larger relative errors than in other situations. This increase in relative errors can be attributed to the reduction in the deviation of signal sensitivities as the two FOVs approach each other, consequently leading to higher retrieval errors. Besides, when both FOVs deviate in the same direction (either

smaller or larger than the true FOVs, dark blue area in Fig. 10), the retrieval errors are relatively lower due to the relatively consistent deviation in signal sensitivity.

IV. Conclusion

We present a novel methodology for profiling water cloud properties by dual-FOV HSRL based on the MC simulations and field observations. Validation of results in future studies should be based on long-term measurements and include additional instruments for collecting supplementary data, such as airborne in situ instruments for cloud properties, Raman lidar for temperature, and differential absorption lidar for humidity. Besides, this technique is limited by the penetration depth of the laser, which makes it difficult to detect the top region of optically thick clouds. Hence, future research should prioritize enhancing the detection depth by either strengthening the energy of the laser (while adhering to human eye safety standards) or improving the capacity to detect weak signals (e.g., via photonic signal stitching). Lidar can detect both aerosol particles and water cloud droplets through the implementation of the dual-FOV HSRL technique. This technique is particularly effective in observing clouds near the cloud base, while radar has a greater penetration capability. Consequently, research on data fusion between the dual-FOV HSRL and cloud radar, which offers a greater penetration depth, looks promising.

Despite some limitations in this work, the dual-FOV HSRL technique allows for directly obtaining the diurnal temporal and vertical distribution of water cloud properties. The case studies presented in this contribution provide additional data with certain relationships between different properties of low-level water clouds in North and East China. In addition, it was found that the subadiabatic assumption matches well with the vertical structure of the water cloud properties in the lower part of the cloud. However, further research incorporating more auxiliary measurements (airborne instruments, balloon-borne samplers, and so on) is necessary to fully understand and characterize the possible data discrepancy compared to the subadiabatic assumption near the cloud top. Moreover, when combined with diurnal profiles of aerosol properties observed by HSRL [56], this technique can contribute significantly to the investigation of aerosol–cloud interactions. Although this study is based on ground-based instruments, the same methods can be easily implemented on existing airborne or spaceborne HSRLs by simply adding a signal channel with a different FOV size to the original lidar. Altogether, the method and results of this study could have critical implications for reducing uncertainty in water cloud characterization and advancing our understanding of aerosol–cloud interactions.

Appendix

A. Parameterization of the Water Cloud

The modified gamma distribution is widely used as a parameterization solution for the size distribution of water cloud droplets [23], [24], [38], which is

$$n(r) = \frac{N_{\mathrm{d}}}{r_m} \frac{1}{(\gamma-1)!} \left(\frac{r}{r_m}\right)^{\gamma-1} \exp\left(-\frac{r}{r_m}\right) \tag{6}$$

where r is the water droplet radius, N_{d} is the cloud droplet number concentration, r_m is the mode radius, and γ is the shape parameter of the gamma distribution. We select 12.3 for the parameter γ in our study. This value is widely adapted from the data processing of moderate-resolution imaging spectroradiometer (MODIS) [57]. The effective radius of the size distribution r_{eff} and r_m are connected by the following relationship:

$$r_{\mathrm{eff}} = \int n(r) r^3 dr \Big/ \int n(r) r^2 dr = r_m(\gamma + 2). \tag{7}$$

The most important water cloud properties are the extinction coefficient α_c, the effective droplet radius r_{eff}, the LWC, and the cloud droplet number concentration N_{d} [21], [23]. The LWC and N_{d} can be expressed by r_{eff} and α_c, respectively [26]

$$\mathrm{LWC} = \frac{2}{3} \rho_w \alpha_c r_{\mathrm{eff}} \tag{8}$$

$$N_{\mathrm{d}} = \frac{1}{2\pi k} \alpha_c r_{\mathrm{eff}}^{-2} \tag{9}$$

where ρ_w is the density of water. k represents the ratio between the cubic power of the volume mean droplet radius and the cubic power of r_{eff}, which is around 0.75 ± 0.15 for continental air masses and around 0.8 for marine stratocumulus [58]. Therefore, α_c and r_{eff} act as the two most critical properties in the water cloud retrieval.

The subadiabatic assumption considers a reduction in LWC due to evaporation triggered by the entrainment of drier air masses above the cloud top [23]. This assumption is considered more appropriate for the retrieval of low-level water clouds from remote sensing [24], [59], compared to the adiabatic model that holds true under convective conditions. Based on the subadiabatic assumption, water cloud properties could be written as a function related to their values at the reference height (75 m above the cloud base in this study)

$$\alpha_{\mathrm{c}}(z) = \alpha_{\mathrm{c}}(z_{\mathrm{ref}}) \left(\frac{z - z_{\mathrm{b}}}{z_{\mathrm{ref}} - z_{\mathrm{b}}}\right)^{\frac{2}{3}} \tag{10}$$

$$r_{\mathrm{eff}}(z) = r_{\mathrm{eff}}(z_{\mathrm{ref}}) \left(\frac{z - z_{\mathrm{b}}}{z_{\mathrm{ref}} - z_{\mathrm{b}}}\right)^{\frac{1}{3}} \tag{11}$$

where z is the cloud height, z_{ref} is the reference height, and z_{b} is the cloud base height.

B. Data Processing of Cloud Radar

The LWC can be derived by the cloud radar reflectivity Z [60], which is expressed as

$$\mathrm{LWC} = aZ^{0.5} \tag{12}$$

where the constant a can be obtained by airborne in situ instruments. In this study, the value of 1.04 was adopted for a based on data obtained from previous aircraft observations conducted over Beijing [61]. Then, the effective radius (r_{eff}) can be calculated by [18]

$$r_{\mathrm{eff}} = \left(\frac{3\mathrm{LWC}}{4\pi\rho_l N_{\mathrm{d}} \exp\left(4.5\sigma_x^2\right)}\right)^{1/3} \exp\left(2.5\sigma_x^2\right) \tag{13}$$

where ρ_l is the density of water, N_{d} is the cloud droplet number concentration, and $\sigma_x = 0.35$. Although N_{d} is usually

assumed to be constant, the value of N_d obtained from dual-FOV HSRL has been utilized in (13) to reduce the uncertainty of r_{eff} retrieved by cloud radar observations in this study.

ACKNOWLEDGMENT

The authors want to thank insightful discussions from Dr. Albert Ansmann about this work. They thank the Copernicus Climate Change Service for the reanalysis data and the Institute of Atmospheric Physics, China, for providing them with the field experiment site.

REFERENCES

[1] J. Li et al., "Long-term variation of cloud droplet number concentrations from space-based LiDAR," *Remote Sens. Environ.*, vol. 213, pp. 144–161, Aug. 2018.

[2] J. Mülmenstädt et al., "An underestimated negative cloud feedback from cloud lifetime changes," *Nature Climate Change*, vol. 11, no. 6, pp. 508–513, Jun. 2021.

[3] P. Forster et al., "The Earth's energy budget, climate feedbacks, and climate sensitivity," in *Climate Change 2021: The Physical Science Basis* (Contribution of Working Group I to the Sixth Assessment Report of the Intergovernmental Panel on Climate Change). Cambridge, U.K.: Cambridge Univ. Press, 2021, pp. 923–1054.

[4] J.-L. Dufresne and S. Bony, "An assessment of the primary sources of spread of global warming estimates from coupled atmosphere–ocean models," *J. Climate*, vol. 21, no. 19, pp. 5135–5144, Oct. 2008.

[5] A. C. Clement, R. Burgman, and J. R. Norris, "Observational and model evidence for positive low-level cloud feedback," *Science*, vol. 325, no. 5939, pp. 460–464, Jul. 2009.

[6] F.-M. Bréon, D. Tanré, and S. Generoso, "Aerosol effect on cloud droplet size monitored from satellite," *Science*, vol. 295, no. 5556, pp. 834–838, Feb. 2002.

[7] D. Rosenfeld, S. Sherwood, R. Wood, and L. Donner, "Climate effects of aerosol-cloud interactions," *Science*, vol. 343, no. 6169, pp. 379–380, Jan. 2014.

[8] E.-S. Chung and B. J. Soden, "Hemispheric climate shifts driven by anthropogenic aerosol–cloud interactions," *Nature Geosci.*, vol. 10, no. 8, pp. 566–571, Aug. 2017.

[9] D. Rosenfeld et al., "Flood or drought: How do aerosols affect precipitation?" *Science*, vol. 321, no. 5894, pp. 1309–1313, Sep. 2008.

[10] N. N. Lata, Z. Cheng, D. Dexheimer, D. Zhang, F. Mei, and S. China, "Vertical gradient of size-resolved aerosol compositions over the Arctic reveals cloud processed aerosol in-cloud and above cloud," *Environ. Sci. Technol.*, vol. 57, no. 14, pp. 5821–5830, Apr. 2023.

[11] C. Zhao et al., "Toward understanding of differences in current cloud retrievals of ARM ground-based measurements," *J. Geophys. Res., Atmos.*, vol. 117, no. D10, p. 206, May 2012.

[12] C. Zhao et al., "Negative aerosol-cloud re relationship from aircraft observations over Hebei, China," *Earth Space Sci.*, vol. 5, no. 1, pp. 19–29, Jan. 2018.

[13] R. Bennartz and J. Rausch, "Global and regional estimates of warm cloud droplet number concentration based on 13 years of Aqua-MODIS observations," *Atmos. Chem. Phys.*, vol. 17, no. 16, pp. 9815–9836, Aug. 2017.

[14] H. Letu et al., "High-resolution retrieval of cloud microphysical properties and surface solar radiation using Himawari-8/AHI next-generation geostationary satellite," *Remote Sens. Environ.*, vol. 239, pp. 1–16, Mar. 2020.

[15] C. Zhao, L. Liu, Q. Wang, Y. Qiu, Y. Wang, and X. Wu, "MMCR-based characteristic properties of non-precipitating cloud liquid droplets at Naqu site over Tibetan Plateau in July 2014," *Atmos. Res.*, vol. 190, pp. 68–76, Jul. 2017.

[16] G. Roy, L. Bissonnette, C. Bastille, and G. Vallée, "Retrieval of droplet-size density distribution from multiple-field-of-view cross-polarized LiDAR signals: Theory and experimental validation," *Appl. Opt.*, vol. 38, no. 24, p. 5202, Aug. 1999.

[17] L. R. Bissonnette and D. L. Hutt, "Multiple scattering LiDAR," *Appl. Opt.*, vol. 29, no. 34, p. 5045, Dec. 1990.

[18] H. Okamoto et al., "Development of a multiple-field-of-view multiple-scattering polarization LiDAR: Comparison with cloud radar," *Opt. Exp.*, vol. 24, no. 26, p. 30053, Dec. 2016.

[19] J. Schmidt, U. Wandinger, and A. Malinka, "Dual-field-of-view Raman LiDAR measurements for the retrieval of cloud microphysical properties," *Appl. Opt.*, vol. 52, no. 11, p. 2235, Apr. 2013.

[20] A. V. Malinka and E. P. Zege, "Possibilities of warm cloud microstructure profiling with multiple-field-of-view Raman LiDAR," *Appl. Opt.*, vol. 46, no. 35, p. 8419, Dec. 2007.

[21] J. Schmidt et al., "Dual-FOV Raman and Doppler LiDAR studies of aerosol-cloud interactions: Simultaneous profiling of aerosols, warm-cloud properties, and vertical wind," *J. Geophys. Res., Atmos.*, vol. 119, no. 9, pp. 5512–5527, May 2014.

[22] J. Yin and A. Porporato, "Diurnal cloud cycle biases in climate models," *Nature Commun.*, vol. 8, no. 1, p. 2269, Dec. 2017.

[23] C. Jimenez, "The dual-field-of-view polarization LiDAR technique: A new concept in monitoring aerosol effects in liquid-water clouds—Theoretical framework," *Atmos. Chem. Phys.*, vol. 20, no. 23, pp. 15247–15263, Dec. 2020.

[24] D. P. Donovan, H. Klein Baltink, J. S. Henzing, S. R. de Roode, and A. P. Siebesma, "A depolarisation LiDAR-based method for the determination of liquid-cloud microphysical properties," *Atmos. Meas. Techn.*, vol. 8, no. 1, pp. 237–266, Jan. 2015.

[25] D. Merk, H. Deneke, B. Pospichal, and P. Seifert, "Investigation of the adiabatic assumption for estimating cloud micro- and macrophysical properties from satellite and ground observations," *Atmos. Chem. Phys.*, vol. 16, no. 2, pp. 933–952, Jan. 2016.

[26] J. W. Hair et al., "Airborne high spectral resolution LiDAR for profiling aerosol optical properties," *Appl. Opt.*, vol. 47, no. 36, p. 6734, Dec. 2008.

[27] N. Wang et al., "Development of ZJU high-spectral-resolution LiDAR for aerosol and cloud: Feature detection and classification," *J. Quant. Spectrosc. Radiat. Transf.*, vol. 261, Mar. 2021, Art. no. 107513.

[28] J. Ke et al., "Development of China's first space-borne aerosol-cloud high-spectral-resolution LiDAR: Retrieval algorithm and airborne demonstration," *PhotoniX*, vol. 3, no. 1, p. 17, Dec. 2022.

[29] N. Wang et al., "Dual-field-of-view high-spectral-resolution LiDAR: Simultaneous profiling of aerosol and water cloud to study aerosol–cloud interaction," *Proc. Nat. Acad. Sci. USA*, vol. 119, no. 10, Mar. 2022, Art. no. e211075611.

[30] P. Piironen and E. W. Eloranta, "Demonstration of a high-spectral-resolution LiDAR based on an iodine absorption filter," *Opt. Lett.*, vol. 19, no. 3, p. 234, Feb. 1994.

[31] B. Jiang, S. Zhu, L. Ren, L. Shi, and X. Zhang, "Simultaneous ultraviolet, visible, and near-infrared continuous-wave lasing in a rare-Earth-doped microcavity," *Adv. Photon.*, vol. 4, no. 4, Jul. 2022, Art. no. 046003.

[32] Y. Li, W. Zheng, and F. Huang, "All-silicon photovoltaic detectors with deep ultraviolet selectivity," *PhotoniX*, vol. 1, no. 1, p. 15, Jun. 2020.

[33] J. C. Ramella-Roman, S. A. Prahl, and S. L. Jacques, "Three Monte Carlo programs of polarized light transport into scattering media: Part I," *Opt. Exp.*, vol. 13, no. 12, pp. 4420–4438, 2005.

[34] D. Liu et al., "LiDAR remote sensing of seawater optical properties: Experiment and Monte Carlo simulation," *IEEE Trans. Geosci. Remote Sens.*, vol. 57, no. 11, pp. 9489–9498, Nov. 2019.

[35] Q. Liu et al., "A semianalytic Monte Carlo simulator for spaceborne oceanic LiDAR: Framework and preliminary results," *Remote Sens.*, vol. 12, no. 17, p. 2820, Aug. 2020.

[36] A. V. Malinka and E. P. Zege, "Analytical modeling of Raman LiDAR return, including multiple scattering," *Appl. Opt.*, vol. 42, no. 6, pp. 1075–1081, 2003.

[37] *U.S. Standard Atmosphere 1976*, U.S. Government Printing Office, NOAA, Washington, DC, USA, 1976.

[38] N. L. Miles, J. Verlinde, and E. E. Clothiaux, "Cloud droplet size distributions in low-level stratiform clouds," *J. Atmos. Sci.*, vol. 57, no. 2, pp. 295–311, Jan. 2000.

[39] L. R. Bissonnette, "Multiple-scattering LiDAR equation," *Appl. Opt.*, vol. 35, no. 33, p. 6449, Nov. 1996.

[40] J. Cunningham, Y. Zheng, T. Subramanian, and M. Almekkawy, "Improved real-time capability for nonlinear seperable harmonic filtering of ultrasound images using a damped regularization method with in-vivo results," in *Proc. 40th Annu. Int. Conf. IEEE Eng. Med. Biol. Soc. (EMBC)*, Jul. 2018, pp. 891–894.

[41] X. Shen et al., "Development of ZJU high-spectral-resolution LiDAR for aerosol and cloud: Calibration of overlap function," *J. Quant. Spectrosc. Radiat. Transf.*, vol. 257, Dec. 2020, Art. no. 107338.
[42] G. L. Stephens, "Cloud physics from space," *Quart. J. Roy. Meteorolog. Soc.*, vol. 145, no. 724, pp. 2854–2875, Jun. 2019.
[43] S. Zhou, J. Yang, W.-C. Wang, C. Zhao, D. Gong, and P. Shi, "An observational study of the effects of aerosols on diurnal variation of heavy rainfall and associated clouds over Beijing–Tianjin–Hebei," *Atmos. Chem. Phys.*, vol. 20, no. 9, pp. 5211–5229, May 2020.
[44] R. A. Houze, "Cloud microphysics," in *International Geophysics*. New York, NY, USA: Academic, 2014, pp. 47–76.
[45] Z. Wang and K. Sassen, "Cloud type and macrophysical property retrieval using multiple remote sensors," *J. Appl. Meteorol.*, vol. 40, no. 10, pp. 1665–1682, Oct. 2001.
[46] K. Sassen and Z. Wang, "Classifying clouds around the globe with the CloudSat radar: 1-year of results," *Geophys. Res. Lett.*, vol. 35, no. 4, p. 805, Feb. 2008.
[47] A. McComiskey et al., "An assessment of aerosol-cloud interactions in marine stratus clouds based on surface remote sensing," *J. Geophys. Res., Atmos.*, vol. 114, no. D9, p. 203, May 2009.
[48] J.-Y. Chun, R. Wood, P. Blossey, and S. J. Doherty, "Microphysical, macrophysical, and radiative responses of subtropical marine clouds to aerosol injections," *Atmos. Chem. Phys.*, vol. 23, no. 2, pp. 1345–1368, Jan. 2023.
[49] S. Twomey, "The influence of pollution on the shortwave albedo of clouds," *J. Atmos. Sci.*, vol. 34, no. 7, pp. 1149–1152, Jul. 1977.
[50] C. H. Twohy et al., "Evaluation of the aerosol indirect effect in marine stratocumulus clouds: Droplet number, size, liquid water path, and radiative impact," *J. Geophys. Res., Atmos.*, vol. 110, no. D8, p. 203, Apr. 2005.
[51] D. Rosenfeld, Y. Zhu, M. Wang, Y. Zheng, T. Goren, and S. Yu, "Aerosol-driven droplet concentrations dominate coverage and water of oceanic low-level clouds," *Science*, vol. 363, no. 6427, Feb. 2019, Art. no. eaav056.
[52] K. M. Doulgeris, V. Vakkari, E. J. O'Connor, V.-M. Kerminen, H. Lihavainen, and D. Brus, "Influence of air mass origin on microphysical properties of low-level clouds in a subarctic environment," *Atmos. Chem. Phys.*, vol. 23, no. 4, pp. 2483–2498, Feb. 2023.
[53] J. Dionne et al., "Modelling the relationship between liquid water content and cloud droplet number concentration observed in low clouds in the summer Arctic and its radiative effects," *Atmos. Chem. Phys.*, vol. 20, no. 1, pp. 29–43, Jan. 2020.
[54] K. Mansour et al., "Phytoplankton impact on marine cloud microphysical properties over the northeast Atlantic Ocean," *J. Geophys. Res., Atmos.*, vol. 127, no. 10, May 2022, Art. no. e2021JD03635.
[55] R. C. Braga et al., "Further evidence for CCN aerosol concentrations determining the height of warm rain and ice initiation in convective clouds over the Amazon basin," *Atmos. Chem. Phys.*, vol. 17, no. 23, pp. 14433–14456, Dec. 2017.
[56] D. Xiao et al., "Simultaneous profiling of dust aerosol mass concentration and optical properties with polarized high-spectral-resolution LiDAR," *Sci. Total Environ.*, vol. 872, May 2023, Art. no. 162091.
[57] R. Bennartz, "Global assessment of marine boundary layer cloud droplet number concentration from satellite," *J. Geophys. Res., Atmos.*, vol. 112, no. D2, p. 201, Jan. 2007.
[58] M. Lu and J. H. Seinfeld, "Effect of aerosol number concentration on cloud droplet dispersion: A large-eddy simulation study and implications for aerosol indirect forcing," *J. Geophys. Res., Atmos.*, vol. 111, no. D2, p. 207, Jan. 2006.
[59] P. Minnis et al., "CERES MODIS cloud product retrievals for edition 4—Part I: Algorithm changes," *IEEE Trans. Geosci. Remote Sens.*, vol. 59, no. 4, pp. 2744–2780, Apr. 2021.
[60] R. T. Austin and G. L. Stephens, "Retrieval of stratus cloud microphysical parameters using millimeter-wave radar and visible optical depth in preparation for CloudSat: 1. Algorithm formulation," *J. Geophys. Res., Atmos.*, vol. 106, no. D22, pp. 28233–28242, Nov. 2001.
[61] L. Wang, C. Li, Z. Yao, Z. Zhao, Z. Han, and Q. Wei, "Application of aircraft observations over Beijing in cloud microphysical property retrievals from CloudSat," *Adv. Atmos. Sci.*, vol. 31, no. 4, pp. 926–937, Jul. 2014.

Kai Zhang received the B.S. degree in optical engineering from the College of Optical Science and Engineering, Zhejiang University, Hangzhou, China, in 2019, where he is currently pursuing the Ph.D. degree.

His research interests include lidar and remote sensing.

Lingyun Wu, photograph and biography not available at the time of publication.

Daniel Rosenfeld, photograph and biography not available at the time of publication.

Detlef Müller, photograph and biography not available at the time of publication.

Chengcai Li, photograph and biography not available at the time of publication.

Chuanfeng Zhao, photograph and biography not available at the time of publication.

Eduardo Landulfo, photograph and biography not available at the time of publication.

Cristofer Jimenez, photograph and biography not available at the time of publication.

Shuaibo Wang, photograph and biography not available at the time of publication.

Xianzhe Hu, photograph and biography not available at the time of publication.

Weize Li, photograph and biography not available at the time of publication.

Xiaotao Li, photograph and biography not available at the time of publication.

Yao Sun, photograph and biography not available at the time of publication.

Sihan Liu, photograph and biography not available at the time of publication.

Lan Wu, photograph and biography not available at the time of publication.

Xueping Wan, photograph and biography not available at the time of publication.

Wentai Chen, photograph and biography not available at the time of publication.

Chong Liu, photograph and biography not available at the time of publication.

Jian Bai, photograph and biography not available at the time of publication.

Jing Li, photograph and biography not available at the time of publication.

Wenbo Sun, photograph and biography not available at the time of publication.

Sivakumar Venkataraman, photograph and biography not available at the time of publication.

Yudi Zhou, photograph and biography not available at the time of publication.

Zhiji Deng, photograph and biography not available at the time of publication.

Ming Liu , photograph and biography not available at the time of publication.

Miao Cheng, photograph and biography not available at the time of publication.

Zhewei Fu, photograph and biography not available at the time of publication.

Weilin Pan, photograph and biography not available at the time of publication.

Dong Liu received the bachelor's and Ph.D. degrees from the Department of Optical Engineering, Zhejiang University, Hangzhou, China, in 2005 and 2010, respectively.

From 2010 to 2012, he held a post-doctoral position at the National Aeronautics and Space Administration (NASA), Washington, DC, for two years. In September 2012, he became a Faculty Member at the Department of Optical Engineering, Zhejiang University, where he became a Full Professor in 2017. He is currently the Deputy Dean of the College of Optical Science and Engineering, Zhejiang University, and the Deputy Director of the State Key Laboratory of Extreme Photonics and Instrumentation. His research interests are applied optics and optical instrumentation, including interferometry, machine vision, and lidar. He is developing lidar systems for atmosphere and ocean study, and further space application. He is the author of about 100 scientific articles in Proceedings of the National Academy of Sciences (PNAS), PhotoniX, and so on, and three books. He holds more than 40 patents and gives more than 50 keynote/invited talks.